DOI:
10.1021/acs.analchem.9b05759

Document Version
Publisher's PDF, also known as Version of record

analytical chemistry

pubs.acs.org/ac

Article

Synchrotron Photothermal Infrared Nanospectroscopy of Drug-Induced Phospholipidosis in Macrophages

Ka Lung Andrew Chan,* Ioannis Lekkas, Mark D. Frogley, Gianfelice Cinque, Ali Altharawi, Gianluca Bello, and Lea Ann Dailey

Cite This: *Anal. Chem.* 2020, 92, 8097−8107

Read Online

ACCESS | Metrics & More | Article Recommendations | Supporting Information

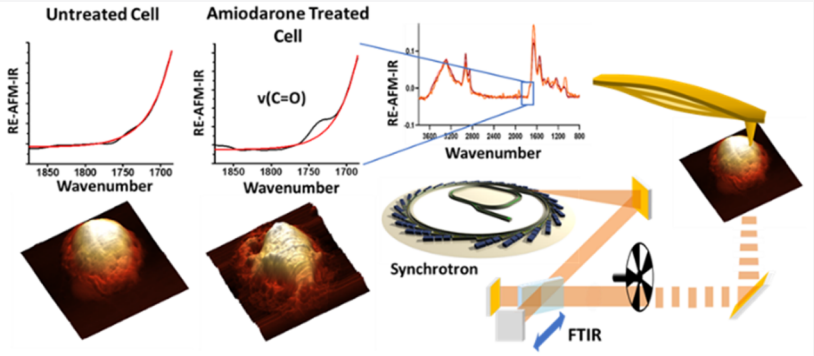

ABSTRACT: Synchrotron resonance-enhanced infrared atomic force microscopy (RE-AFM-IR) is a near-field photothermal vibrational nanoprobe developed at Diamond Light Source (DLS), capable of measuring mid-infrared absorption spectra with spatial resolution around 100 nm. The present study reports a first application of synchrotron RE-AFM-IR to interrogate biological soft matter at the subcellular level, in this case, on a cellular model of drug-induced phospholipidosis (DIPL). J774A-1 macrophages were exposed to amiodarone (10 μM) or medium for 24 h and chemically fixed. AFM topography maps revealed amiodarone-treated cells with enlarged cytoplasm and very thin regions corresponding to collapsed vesicles. IR maps of the whole cell were analyzed by exploiting the RE-AFM-IR overall signal, i.e., the integrated RE-AFM-IR signal amplitude versus AFM-derived cell thickness, also on lateral resolution around 100 nm. Results show that vibrational band assignment was possible, and all characteristic peaks for lipids, proteins, and DNA/RNA were identified. Both peak ratio and unsupervised chemometric analysis of RE-AFM-IR nanospectra generated from the nuclear and perinuclear regions of untreated and amiodarone-treated cells showed that the perinuclear region (i.e., cytoplasm) of amiodarone-treated cells had significantly elevated band intensities in the regions corresponding to phosphate and carbonyl groups, indicating detection of phospholipid-rich inclusion bodies typical for cells with DIPL. The results of this study are of importance to demonstrate not only the applicability of Synchrotron RE-AFM-IR to soft biological matters with subcellular spatial resolution but also that the spectral information gathered from an individual submicron sample volume enables chemometric identification of treatment and biochemical differences between mammalian cells.

Resonance-enhanced infrared atomic force microscopy (RE-AFM-IR) is a near-field IR microscope optimized at the MIRIAM beamline B22 of Diamond Synchrotron Light Source (DLS).[1] In brief, it exploits photothermal expansion due to infrared absorption to break the diffraction limit, generating IR absorption spectra with spatial resolution around 100 nm, depending on the sample's geometry and thermal properties. In contrast to commercial near-field AFM-IR technology[2] utilizing pulsed lasers which scan single wavelengths one at a time to obtain a spectrum,[3] the RE-AFM-IR at B22 of DLS operates via broadband synchrotron radiation (SR), allowing all wavelengths in the mid-IR region to be measured simultaneously. Full FTIR spectral measurements can be advantageous especially for the study of biological samples where spectral differences between cell types or disease states can be complex.

In the RE-AFM-IR end station at B22 of Diamond, SR passes through the all in-vacuum beamline and FTIR interferometer (Bruker vertex 80V) followed by a mechanical chopper before being focused onto the sample through a high numerical aperture Cassegrain objective. In brief, we used an

Received: December 20, 2019
Accepted: May 12, 2020
Published: May 12, 2020

https://dx.doi.org/10.1021/acs.analchem.9b05759
Anal. Chem. 2020, 92, 8097−8107

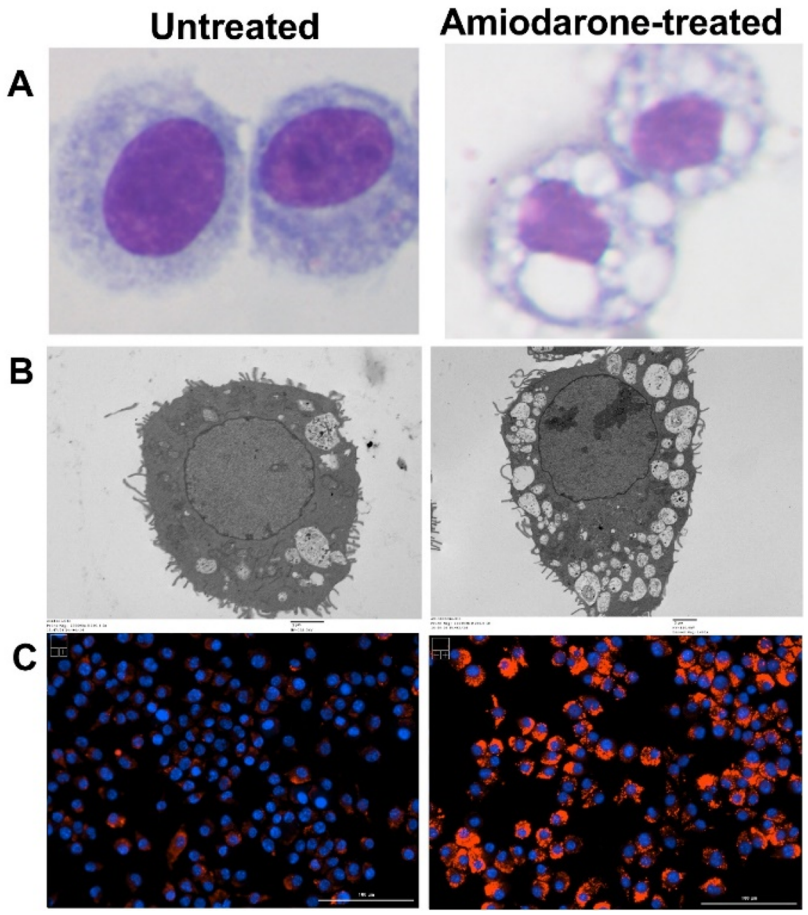

Figure 1. Microscopic characterization of untreated and amiodarone-treated J774A.1 cells. The spatial distribution of phospholipid inclusion bodies is shown by (A) light microscopy with hematoxylin and eosin staining, (B) TEM, and (C) fluorescence microscopy with LipidTOX Red.

atomic force microscope (Nanonics MV1000) to detect, statically, in each point of the sample, the mechanical change following a local thermal variation due to an initial IR absorption. The mechanical chopper frequency is tuned to the contact resonance frequency of the AFM cantilever in order to resonantly enhance the cantilever oscillation and therefore increase the photothermal IR signal from submicron areas.[1] Previous work on polystyrene films and cyanoacrylate ridge microsamples demonstrated that synchrotron RE-AFM-IR nanospectroscopy can acquire full mid-IR absorption spectra at around 100 nm spatial resolution, which is well below the limit of diffraction achievable by far-field FTIR imaging, micro-ATR FTIR imaging, or other solid immersion FTIR imaging approaches.[4−8]

In this work, the broadband SR RE-AFM-IR method, which covered the entire mid-IR spectral range, was used for the first time to study subcellular regions within a whole mammalian cell. Specifically, a macrophage model of drug-induced phospholipidosis (DIPL) was chosen to interrogate the strengths and limitations of the DLS instrument, because cells with DIPL develop 100−2400 nm size phospholipid-rich inclusion bodies in their cytosol in response to treatment with cationic, amphiphilic drugs (CADs).[9] Amiodarone, an antiarrhythmic agent, is commonly used as a model compound to study DIPL, and conventional characterization methods include light microscopy, transmission electron microscopy, and fluorescence microscopy (Figure 1). The pronounced accumulation of cytosolic phospholipids in DIPL led to the question of whether the high spatial resolution of RE-AFM-IR could be exploited to molecularly characterize the distribution of cytosolic phospholipid inclusion bodies in amiodarone-treated macrophages, without the need for sample staining required by most imaging techniques. It was postulated that the 100−2400 nm phospholipid-rich inclusion bodies would be detectable as their size and unique chemical signature should be distinctive from that of the cytosol of healthy, untreated cells. Furthermore, seamless spectral acquisition across the 4000 to 800 cm^{-1} range with a broadband illumination source, i.e., SR, was used to enable direct comparisons via multispectral analysis and spectral fidelity as guaranteed by FTIR spectroscopy: to our knowledge such a broad spectral range is not achievable continuously and simultaneously by laser sources for AFM-IR research.

Recently, biological samples were measured using synchrotron infrared nanospectroscopy across cytospun cells,[10] based on a near-field scattering signal from a metal coated AFM tip (s-SNOM).[11] The method can obtain broadband IR spectra from nanosize areas, but demonstrated spectra of biological samples were limited to the fingerprint region and were highly dependent on the surface enhancement effect, i.e., for thin layers of samples and heavily depending on the tip quality.[12] In contrast, our work measures the photothermal effect, where the signal produces a true and broadband FTIR spectrum, and provides a bulk measurement beyond the first few tens of nanometers thick surface layer of the whole mammalian cell,

https://dx.doi.org/10.1021/acs.analchem.9b05759
Anal. Chem. 2020, 92, 8097−8107

deposited on the substrate in a way similar to standard microscopy.

Randomly selected untreated (UT) and amiodarone-treated (AM) cells were characterized via SR RE-AFM-IR maps. The integrated RE-AFM-IR signal amplitude (due to all IR wavelengths absorption with no spectral discrimination) was used as it can be rapidly acquired during topography maps and is directly related to morphological features of the cell, providing insight into the minimum sample thickness required to generate RE-AFM-IR spectra of sufficiently high signal-to-noise ratio (SNR) for analysis. From these spectra, bands characteristic for cellular components, such as lipids, proteins, and nucleic acids, were evaluated across the cells to distinguish areas of characteristic chemical composition at a high spatial resolution. Finally, band ratio analysis and principle component analysis of the collected spectra from the nuclear and perinuclear regions of the cells were performed to interrogate differences between untreated and amiodarone-treated groups.

METHODS

Materials. Amiodarone hydrochloride was purchased from Sigma-Aldrich (Dorset, UK). All other materials were of analytical grade.

Cell Culture and Amiodarone Treatment. J774A.1 cells (passage 6) were subcultured in a humidified atmosphere of 5% CO_2 at 37 °C. Culture media consisted of high glucose Dulbecco's modified Eagle's medium (DMEM; Gibco, Life Technologies, UK) supplemented with 10% fetal bovine serum (FBS; Gibco, Life Technologies, UK), 1 μg/mL streptomycin and penicillin (Gibco, Life Technologies, UK), and 1 mM sodium pyruvate (Gibco, Life Technologies, UK). Cells (1×10^6) were seeded on the surface of 5 cm^2 zinc sulfide windows and cultured overnight. One of the samples (untreated cells; UT) received just fresh medium, while a second sample (amiodarone-treated cells; AM) was incubated with fresh cell culture medium containing 10 μM amiodarone hydrochloride for 48 h. At the end of the treatment period, medium was aspirated, and cells were washed 3× with phosphate buffered saline (PBS). Cells were fixed with 4% (v/v) paraformaldehyde for 30 min at room temperature. The fixative was then aspirated, washed 3× with isotonic saline, and stored in saline at 4 °C until use. Prior to sample analysis, fixed cells were washed 3× in distilled water and air-dried.

RE-AFM-IR Spectroscopy. SR illumination is relayed from the B22 bending magnet IR source at Diamond Light Source (www.diamond.ac.uk/B22) and into an interferometer (Bruker Vertex 80V, with broadband KBr beam splitter) via the MIRIAM beamline B22 mirror optics.[13] Spectral characteristics of the SRIR beam can be found at the Web site.[14] The IR light is modulated through a customized high-speed chopper with a 200 slot disc (modified from a Scitec Instruments), operating in vacuum[1] and with a 50% duty cycle. A light chopping frequency at around 70 kHz was used and tuned to the specific tip contact resonance at each sample position. Following tuning, the chopper frequency stabilized in via a closed loop control system (Delta Tau Geobrick), with fine adjustment of the resonance frequency obtained within a precision of ±100 Hz. The chopper tuning process for the measurements shown in this work needed an average of 2 min.

After the chopper, the modulated SRIR beam is passed out of vacuum through a broadband IR window (KBr) and via N_2 purged optics into the infinity corrected microscope from below the sample and focused at the AFM tip position using a 15× Cassegrain objective (Agilent, NA = 0.62). Full SR broadband illumination with a total power less than 1 mW covering the whole mid-IR range from 7000 to 400 cm^{-1} was provided at the Cassegrain focal point, which is optically the demagnified image of the SRIR beam previously focused at a chopper slot. The upper wavenumber limit of the spectral illumination (near-IR) was set by a KBr beamsplitter and exit window, while the lower limit was dictated by the sample substrate (ZnS 1 mm thick). A Nanonics MV1000 AFM mounted onto a X-Y piezo controlled sample stage (PI) was used to, respectively, scan the sample under the AFM tip and bring it to the focus of the IR beam. The photothermal expansion (namely the deflection signal from the in-contact AFM cantilever) was recovered using digital lock-in amplification (Signal Recovery 7280). Typically, a 200 μs time constant was used when operating the FTIR interferometer at a 2.5 kHz scanner velocity (referred to as a 633 nm laser sampling the FTIR). A RE-AFM-IR signal with an amplitude of around 2 mV at the lock in amplifier was typically usable for nanospectroscopy, a signal which was then fed into the FTIR acquisition. Single channel sample spectra were collected at 16 cm^{-1} spectral resolution with 512 scans averaging. This is equivalent to ca. 1 interferogram acquired per second, which is Fast Fourier Transformed online into an RE-AFM-IR spectral scan for averaging at the same rate. Each spectrum (usable from 4000 to 900 cm^{-1}) took approximately 8.5 min of acquisition time for an acceptable SNR (approximately 10 min including chopper tuning). The spectra are not normalized to the (fixed) SR beam spectral intensity or the instrument throughput spectrum, as would typically be done for laser-based AFM-IR. Only changes to band ratios and band intensities across different sample regions are therefore analyzed for biochemical contrast.

Cell Selection Criteria. Adherent J774A.1 cells on the IR substrate were visualized with an optical microscope focused at the surface plane. Four individual cells from the UT group and six from the AM group were selected according to the same criteria: all cells were chosen spatially separated from other cells in order to avoid effects of clustering on the surface topography. Furthermore, an attempt was made to choose cells of average size with respect to the total cell population to avoid biased selection of necrotic or apoptotic cells. Optical images of selected cells can be viewed in the Supporting Information (Figure S1). Following selection, AFM imaging was used to confirm that the cell nuclear region was homogeneously distributed, i.e., the cell was not undergoing apoptosis and/or nuclear degradation (Figure S2).

SR-FTIR Microscopy. SR-FTIR microscopy was carried out at the B22 beamline (MIRIAM) of the DLS synchrotron facility. The system comprises a Vertex 80V FTIR spectrometer and a Hyperion 3000 microscope system (Bruker Optics) with a 36× Cassegrain objective (Newport, NA = 0.5) and a matching condenser. The same cell samples (fixed on ZnS windows) were used for both SR-FTIR and SR RE-AFM-IR measurements. Spectra were collected from cells positioned in the middle of the ZnS window using a 10 μm × 10 μm slit size at 4 cm^{-1} spectral resolution and 128 scans in transmission mode (ca. 20 s per cell).

Spectral Analysis. SR RE-AFM-IR absorption spectra were cropped from 3800 to 900 cm^{-1} before vector normalization using the OPUS software version 7.8 (Bruker Optics). Band intensities were calculated by integrating the

https://dx.doi.org/10.1021/acs.analchem.9b05759
Anal. Chem. 2020, 92, 8097−8107

area under the RE-AFM-IR spectrum, with respect to a local baseline, across specific wavenumber ranges that represent the various chemical components. Band ratios were calculated with respect to the area under the H-stretching region of the spectrum above the CH stretching mode (3745−3020 cm^{-1}), which was found to be relatively consistent across all samples. Further details of this analysis are provided in Figure S3 of the Supporting Information. Principle component analysis (PCA) was applied to each set of spectra using PyChem chemometric software (version 3.0.5 g),[15] after preprocessing (13 point smoothing, second derivative).

Statistics. Comparisons between treated and untreated cells in the perinuclear and nuclear regions were performed using two-way ANOVA with a Tukey correction for multiple comparisons using Graphpad Prism (version 8.1.2). Comparisons between averaged values of treated and nontreated cells were performed with a two-way unpaired Student's *t*-test (Microsoft Excel, 2013). P-values of <0.05 were considered significant.

RESULTS

Assessment of UT and AM Cell Topography. All cells studied were chosen based on the optical image based on the criteria that they were individually representative of the cell population, i.e., spatially separated from other cells and were roughly of average size (Supporting Information, Figure S1). AFM topography scans (Figure 2 and Figure S2) showed that untreated cells (UT1-4) were very similar in size, shape, and height, while amiodarone-treated cells (AM1-6) were larger and with a heterogeneous, thinly spread cytosolic region. Evidence of significant amiodarone-induced vacuolation could be observed as very thin regions in the cytosol, which were attributed to collapsing vacuoles after the fixation and drying of the cells.

RE-AFM-IR Profiles of Cell Cross Sections. Averaged SR RE-AFM-IR spectra from 15 to 20 scan points across three cells from each group (UT vs AM) were compared to a transmission SR-FTIR spectrum generated from single cells on the same sample slides (Figure 3). In general, the SNR of the RE-AFM-IR spectra was lower than that of the transmission FTIR spectrum as the RE-AFM-IR instrument obtains its signal from a sample volume that is several orders of magnitude smaller than the SR-FTIR measurement. Nonetheless, the spectra generated from both techniques show a high degree of similarity. One unexpected but marked difference was observed in the relative intensity of the amide I and II peaks of the UT cell group (Figure 3A). Uncharacteristically, the amide I peak amplitude of UT cells was observed to be equal to or weaker than the amide II peak amplitude. As the microFTIR spectra of the cell did not show the same difference, this effect may be a genuine nanometric biochemical contrast or, more likely, an artifact related to the nearfield photothermal detection. We assign the reduced relative amplitude of amide I to a combination of sublinearity in IR absorption through the 0.5−1.5 μm thick samples, coupled with the cooling effect of the substrate for lower portions of the sample. The nonlinear absorption is a consequence of the Lambert−Beer law and will predominantly affect the strongest, amide I band in the thickest sample regions. Nonlinearity also results in most of the photothermal heat at amide I being generated near the substrate, which is preferentially dissipated by the high thermal conductivity substrate,[16] allowing amide I to appear weaker than amide II.

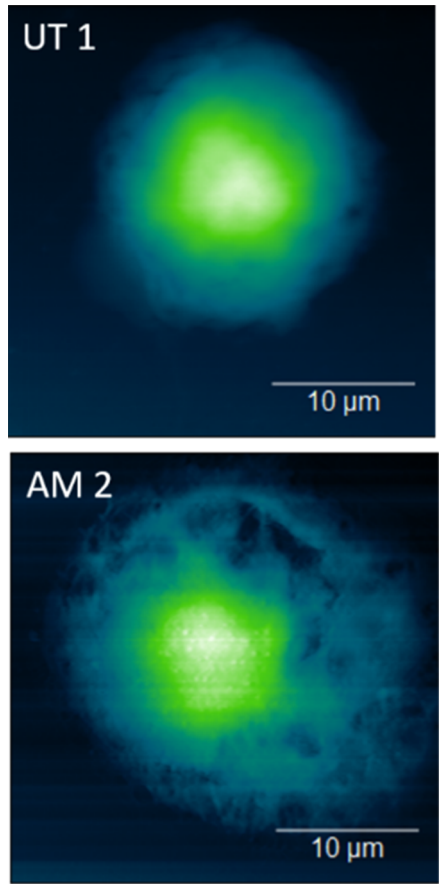

Figure 2. Representative AFM topography image of untreated cells (UT1) and cells treated with amiodarone (AM2) highlighting the differences in morphology between healthy J774A.1 cells and those with DIPL. All other cells are depicted in Figure S2 for completeness.

Cantilever-response-induced reduction of amide I in laser-based RE-AFM-IR has been observed before[17] but in that case only during tip-scanning and not for static acquisitions as performed here. In our static FTIR mode, all IR bands see the same cantilever resonance enhancement. Due to this anomalous behavior, the amide region is not used here to draw any conclusions about the sample biochemistry.

Sequential RE-AFM-IR measurements were then performed every 500 nm across UT1 and AM3 (Figure 4A/F), and heatmaps depicting the signal intensity, i.e., the RE-AFM-IR amplitude at wavenumbers 3800−900 cm^{-1}, are shown for each line (Figure 4C/H). Example spectra from a single scan point of UT1 (scan #8) and AM3 (scan #11) cells are shown in Figure 4E/J. AFM-derived cell topography graphs depict the cell thickness across the scanned region (Figure 4B/G). Using the amide I peak range (1700−1600 cm^{-1}), which represents the presence of protein, it could be seen that while the RE-AFM-IR amplitude generally followed the thickness of cell, the highest amide I intensity values were slightly offset from the highest point of the cell (Figure 4D/I). A similar observation was made by Giliberti et al.[18] using QCL AFM-IR to characterize 34 individual HeLa cells, showing that the highest intensity of the amide I peak was found in the perinuclear region of the cell. In the J774A.1 cells investigated here, a minimal sample thickness of approximately 200 nm was required in order to generate vibrational spectra with a usable SNR. This meant that chemical information from the thinner

https://dx.doi.org/10.1021/acs.analchem.9b05759
Anal. Chem. 2020, 92, 8097−8107

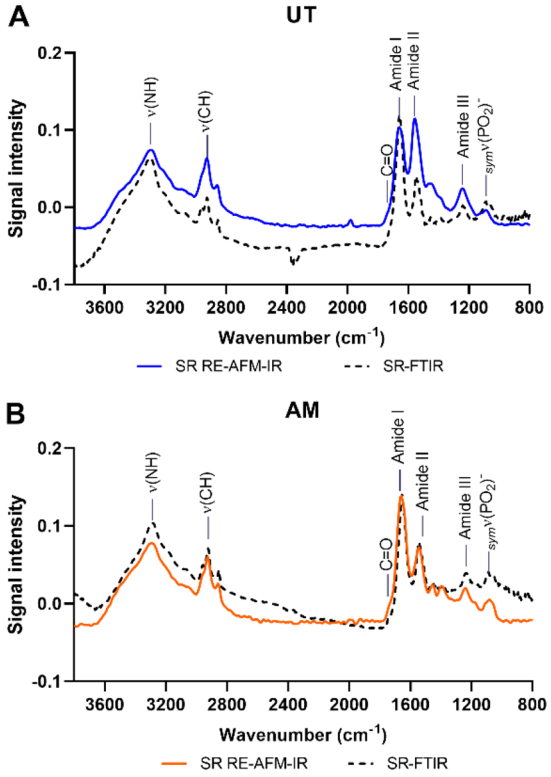

Figure 3. Averaged SR RE-AFM-IR spectra (solid lines) from 15 to 20 scan points in three UT (A) or AM (B) cells compared to SR-FTIR spectra from a single cell (dotted lines). RE-AFM-IR data are vector normalized. SR-FTIR data are scaled/offset for comparison.

regions of the cell, such as the edges and the collapsed vacuoles of AM-treated cells, could not be experimentally retrieved.

Alongside spectra, 2D maps depicting the as-collected and the sample-thickness-normalized integrated RE-AFM-IR amplitude across two untreated (UT1 and UT4) and two amiodarone-treated (AM4 and AM6) cells are shown (Figure 5). These IR maps, in comparison to the topography, visually highlight where the near-field spectroscopic signal is not related to the sample thickness, sometimes showing spatial features around 100 nm found within cells. Because these maps are collected with a fixed IR modulation frequency, optimized at one sample position, strong integrated RE-AFM-IR features can arise not only from a change in the infrared absorption but also from the stiffness contrast (via changes in the cantilever contact resonance frequency) and thermomechanical properties variation across the cell due to its compositional/chemical and physical/structural changes. Major integrated RE-AFM-IR features roughly show corresponding cell morphology and thickness variations, especially visible in the AM cells where the uneven topography, due to cell spreading and collapsed vacuoles, is a characteristic. The normalized amplitude maps were obtained as the ratio of integrated RE-AFM-IR to the topography maps, i.e., the sample thickness. Photothermal IR is a measure of the absorption spectrum,[9,10] and, in first approximation, the Lambert−Beer law would imply direct proportionality with the sample thickness. By dividing the IR signal by the thickness, the normalized integrated RE-AFM-IR maps depict a spatial map of the cells where the contrast is not given by the linearity of the IR absorption but instead dominated by thermo-mechanical physical variation of the cell inner structure.

Chemometric Analysis: Nuclear vs Perinuclear Comparisons. The SR RE-AFM-IR spectral analysis was focused on subcellular regions where a strong signal was obtained, which generally included nuclear and perinuclear areas (see Supplementary Figure S2 for scan maps of all cells). Averaged spectra (3−5 scans) from the nuclear and perinuclear regions were plotted for three UT and AM cells (Figure S4, also shown in Figure 3), again showing the uncharacteristic ratio between the amide I:amide II peak height in both the nuclear and perinuclear regions of the UT cells, which was not typically observed.

Selected spectral features from the nuclear and perinuclear regions of UT and AM cells were then analyzed to gain information on chemical differences between the nucleus and cytosol. Specifically, the peak area ratios between 1) the lipid ν(CH) band (3020−2800 cm^{-1}) and the 3745−3020 cm^{-1} region, 2) the carbonyl ν(C═O) band (1774−1709 cm^{-1}) and the 3745−3020 cm^{-1} region, 3) the $_{asym}\nu(PO_2)^-$ band (1310−1147 cm^{-1}) and the 3745−3020 cm^{-1} region, and 4) the $_{sym}\nu(PO_2)^-$ band (1142−1020 cm^{-1}) and the 3745−3020 cm^{-1} region were analyzed because elevated phospholipid content would likely be reflected in these vibrational modes (Figure 6A). Figure 6A shows that the average peak ratios from the AM-P scans were consistently higher than those of the AM-N region and UT cells for the ν(CH) and ν(C═O) peaks, although it was not observed for the $_{sym}\nu(PO_2)^-$ and $_{asym}\nu(PO_2)^-$ peaks due to the heavy overlaps with protein amide III, carbohydrates, and nucleic acid peaks in this region. However, a ratio between the $_{sym}\nu(PO_2)^-$ peak against the $_{asym}\nu(PO_2)^-$ peak, which overlaps with protein amide III, showed on average an increase for the AM cells but was not statistically significant when comparing AM-P independently due to a large variation in the peak area ratio. This is to be expected considering that the cytosol of the AM cells showed considerable variation in both cell thickness (Figure 4) and chemical composition (Figure 1). It is likely that the AM-P signals are derived from scans positioned in both phospholipid-rich and normal cytosolic regions, resulting in high peak ratio variability. Taken together, the general RE-AFM-IR absorption increases in the ν(CH), ν(C═O), and the $_{sym}\nu(PO_2)^-$ band regions suggest that the perinuclear region of the AM-treated cells contained a higher phospholipid content than the nuclear region, which is not observed in the UT cells.

PCA results, which analyze data across the full IR spectrum, supported observations in the peak area ratio study. Focusing on the principle components (PCs) that described at least 5% of the variance (PC1−4), three PCs of interest were identified (Figure 6B−D). PC3 showed the highest relevance to the central study question, despite a lower contribution to overall variance, because the loading plot indicated that the spectral differences originated from an increase in the lipid ν(CH) band (Figure 6D). The PC3 score plots revealed a clear separation between the nuclear and perinuclear regions of the AM cells and no differences in lipid content in the untreated cells, which is indicative of a higher lipid content in the cytosol of AM but not UT cells and is consistent with the DIPL phenotype. The main source of variance of PC2 was derived from phosphate and protein bands, which were significantly elevated in the perinuclear region of AM cells compared with UT cells. PC1, with the highest contribution to variance, showed a large variability in UT cells, but only minor differences in AM cells. The PC1 loading plot highlights that the differences originated in the amide I and amide II bands,

https://dx.doi.org/10.1021/acs.analchem.9b05759
Anal. Chem. 2020, 92, 8097−8107

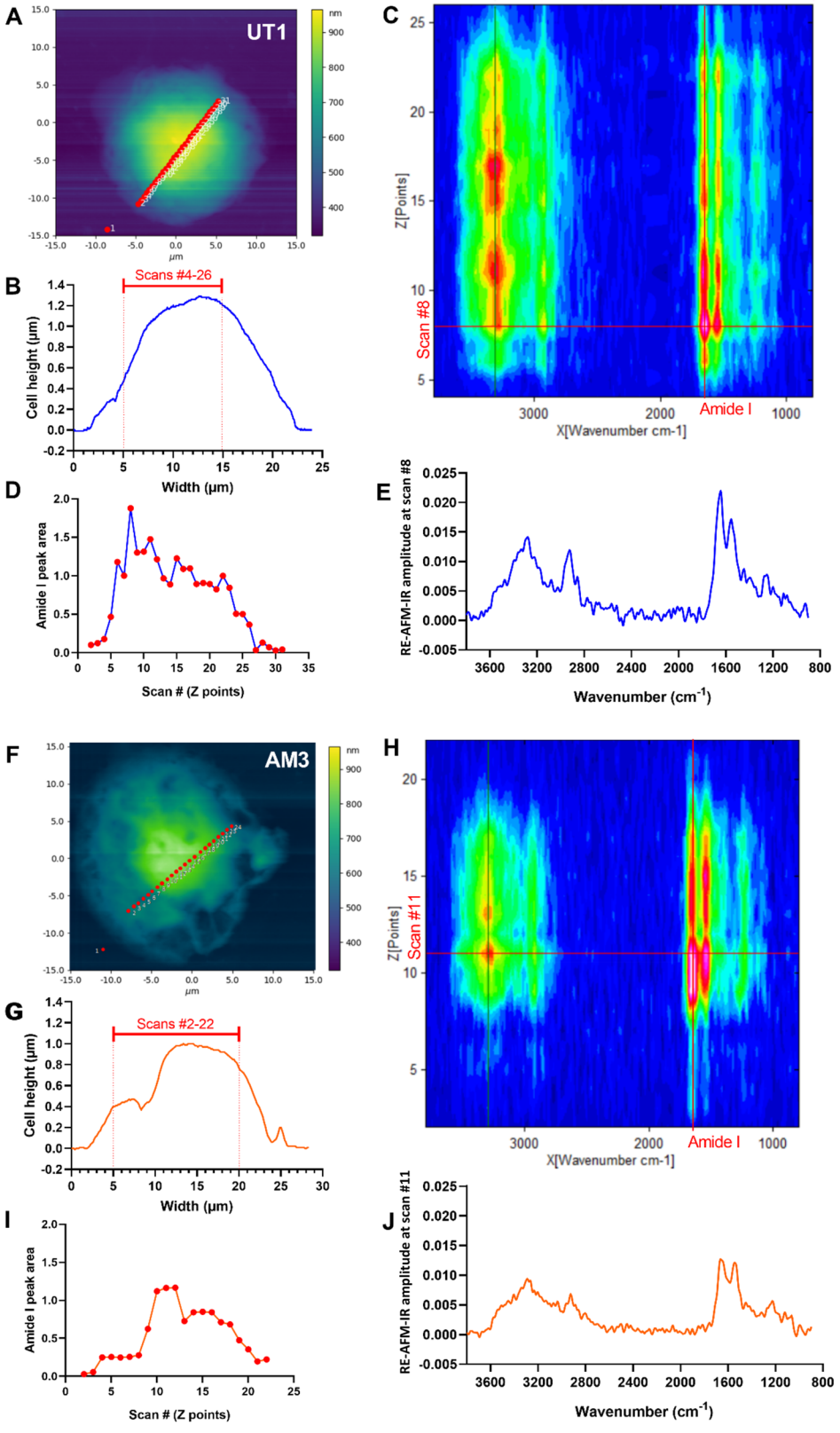

Figure 4. Top panel: SR RE-AFM-IR analysis of UT1: (A) AFM image showing the location (Z-point) of each RE-AFM-IR scan (spacing 500 nm), (B) AFM-derived cell height and width, (C) heatmap of RE-AFM-IR amplitude for wavenumbers 3800−900 cm^{-1} across scans 4-26, (D) amide I peak area (1700−1600 cm^{-1}) for scans 2-31, (E) RE-AFM-IR spectrum (unprocessed) of scan #8. Bottom panel: SR RE-AFM-IR analysis of AM3, (F) AFM image showing the location (Z-point) of each RE-AFM-IR scan (spacing 500 nm), (G) AFM-derived cell height and width, (H) heatmap of RE-AFM-IR amplitude for wavenumbers 3800−900 cm^{-1} for scans 2-22, (I) amide I peak area (1700−1600 cm^{-1}) for scans 2-22, and (J) RE-AFM-IR spectrum (unprocessed) of scan #11.

https://dx.doi.org/10.1021/acs.analchem.9b05759
Anal. Chem. 2020, 92, 8097−8107

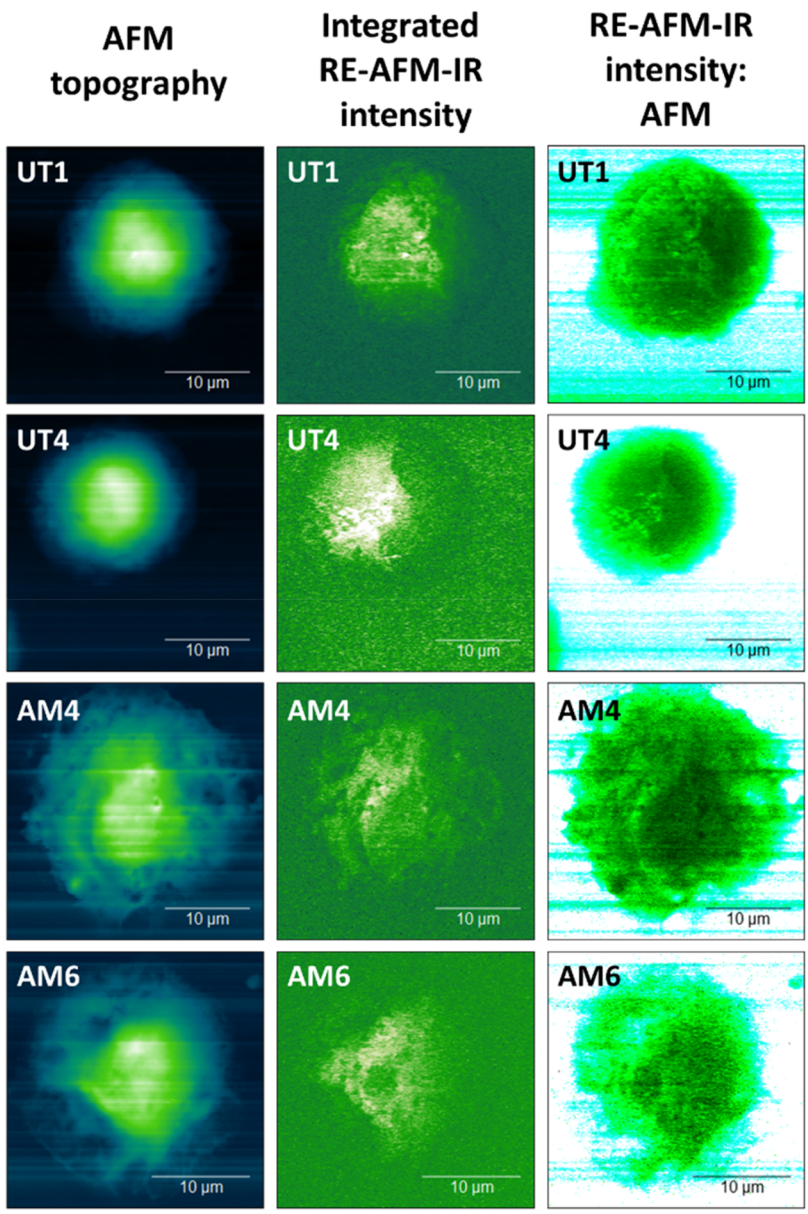

Figure 5. AFM micrographs depicting topology features are compared with overall and normalized integrated RE-AFM-IR amplitude maps for UT1, UT4, AM4, and AM6 cells.

which agrees with previous observations that thicker UT cells often show an unusual amide I:amide II ratio (Figures 3 and 5). The high contribution of PC1 to the overall variance of the data may thus be interpreted as differences in the amide I:amide II ratio resulting from sample thickness rather than treatment-derived chemical differences.

DISCUSSION

This is, to our knowledge, the first successful application of synchrotron-based RE-AFM-IR nanospectroscopy on mammalian cells, where both spatial resolution around 100 nm scale was demonstrated for molecular imaging and FTIR spectral quality, sufficient for chemometric analysis across the entire mid-IR region, was performed at a subcellular level. Typical vibrational features of the cells are all clearly captured providing the biochemical information on the cell in a label-free manner typical of IR spectroscopy. The spectra collected using SR RE-AFM-IR nanospectroscopy showed an intrinsically lower SNR when compared to SR-FTIR microspectroscopy, which is consistent with the submicron volume of sample probed in the AFM-IR configuration. For example, diffraction-limited FTIR imaging generates a signal from a sampling volume per point of approximately 50 μm^3 for a 0.5 μm thick cell sample. With the RE-AFM-IR method, which can access a lateral spatial resolution of ca. 0.1−0.5 μm, depending on the sample, the theoretical probed volume will be at most 0.1 μm^3, i.e., 2−3 orders of magnitude smaller. Normally, the absorption amplitude from such a small volume would not be detectable, but the resonance enhancement is able to increase the signal according to the Q value of the cantilever (in this case generally $\leq$100) and detect it via lock in amplification. Additionally, it should be highlighted that the actual RE-AFM-IR signal is generated by the sample IR absorption and thermal expansion of the area under the tip, which is additional mechanical information on the sample accessible by this non-optical method.

https://dx.doi.org/10.1021/acs.analchem.9b05759
Anal. Chem. 2020, 92, 8097−8107

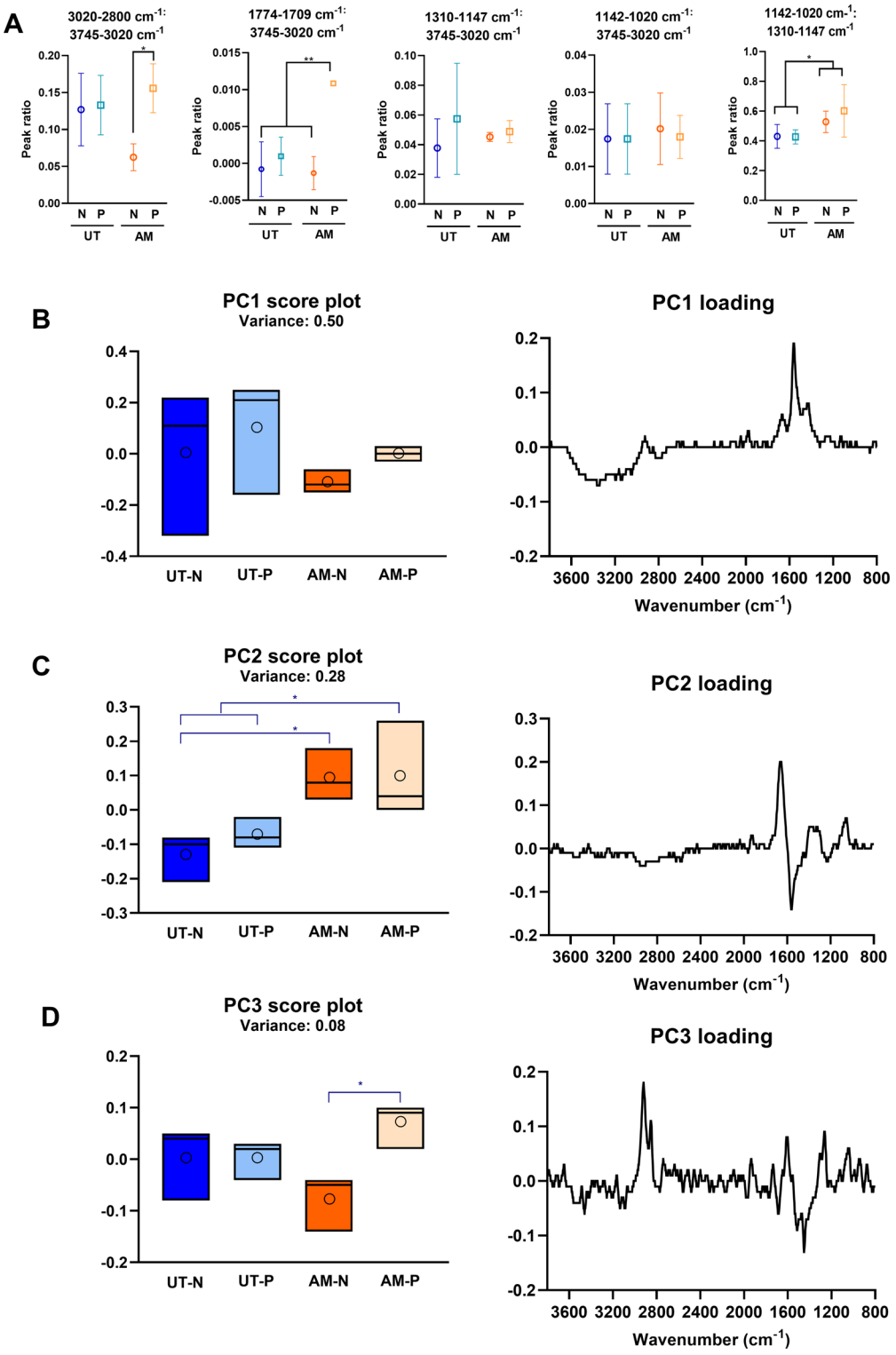

Figure 6. (A) Peak area ratios (mean ± standard deviation) of selected bands of interest from three UT and AM cells: 3020−2800 cm^{-1} (ν(CH)):3745−3020 cm^{-1}, 1774−1709 cm^{-1} (ν(C═O)):3745−3020 cm^{-1}, 1310−1147 cm^{-1} ($_{asym}\nu(PO_2)^-$):3745−3020 cm^{-1}, 1142−1020 cm^{-1} ($_{sym}\nu(PO_2)^-$):3745−3020 cm^{-1}, and 1142−1020 cm^{-1}:1310−1147 cm^{-1}. (B−D) Principle component analysis was performed on the full spectra of UT and AM cells (n = 3), and principle components contributing more than 5% to the variance were shown. The loading plot for each PC is depicted to the right of each score plot summary. Boxes represent the maximum and minimum score, whereby lines within the boxes show the median and open circles mean values. * $p < 0.05$, ** $p < 0.01$.

For quantitative analysis, it is important to be aware of the limitations of the AFM-IR technique. In general for AFM-IR, the signal depends on the mechanical resonant response of the cantilever, and this depends on local mechanical properties of the sample via the contact stiffness and damping at the AFM tip. For data obtained while scanning the tip, such as our integrated RE-AFM-IR maps, or for laser-based AFM-IR imaging data, this can include dynamic and IR wavelength

https://dx.doi.org/10.1021/acs.analchem.9b05759
Anal. Chem. 2020, 92, 8097−8107

dependent mechanical effects.[17] For our static FTIR-based spectral measurements, however, the cantilever resonance quality (and any fluctuations thereof) is identical for all IR wavelengths at each nominal point on the sample. So either by using band ratios or through (e.g., vector) normalization of the spectra, artifacts due to cantilever responsivity are avoided. To obtain the highest signals, we still optimize the IR modulation frequency to the cantilever contact resonance. For spectra obtained at different sample positions, as in our line maps (Figure 4), this optimization greatly reduces the effect of the variation in cantilever responsivity, but absolute IR absorbance cannot be determined and this data are used for qualitative analysis only. A recently developed technique[19] can largely overcome this limitation but requires IR modulation at high frequencies, above the lowest cantilever resonances, which are currently not accessible with our mechanical chopper.

Conventional IR (absorbance) data assumes the Lambert−Beer law, where the calculated absorbance spectrum is proportional to sample thickness and the IR absorption coefficient spectrum. The photothermal signal, in contrast, depends on the IR power absorbed by the sample, which is not, in general, linear with sample thickness. To avoid spectral distortions from this effect, we restrict our analysis to relatively weak IR bands for which the IR absorbed power is approximately linear with sample thickness. The intense amide region of the RE-AFM-IR spectra clearly shows distortions and is rejected from the detailed analysis.

A key advantage of synchrotron broadband IR illumination is related to the full exploitation of Fourier transform interferometry as a multiplexing spectroscopy method.[20] The detection of all IR wavelengths simultaneously, typical of FTIR, is not possible by a QCL laser, which sequentially measures one wavelength at a time and requires a series of devices (with significant power variations) to cover, for example, the fingerprint IR region. Supercontinuum lasers can broadly cover the stretching or fingerprint regions but are suffering from reproducibility issues, e.g., shot by shot variations. Recent works by AFM-IR, e.g., via pulsed OPO lasers, have demonstrated the potential of multispectral analysis on single cells,[21,22] in both cases using separately the stretching and the fingerprint regions. SR FTIR offers seamless spectra in the whole IR region, with sufficient stability and reproducibility to apply chemometric methods, like PCA or HCA, using the whole IR vibrational absorption spectrum. When coupled to RE-AFM-IR, this translates into access to biochemical information at the nanoscale in a complex molecular system like mammalian cells or tissues via assessment of global spectral changes beyond the single band assignment, which is a limitation of the single wavelength approach.

As discussed in the context of the RE-AFM-IR profiles of cell cross sections above, the amide region of the near-field spectra shows anomalous behavior most likely due to the high and nonlinear absorption of IR light through the thicker sample regions combined with sample cooling near the substrate. A recent paper analyzed the sample thickness effect on AFM-IR absorption spectra in terms of nonlinearity.[23] The carbonyl band deviation in intensity from the Lambert−Beer law was identified as the one that can show a non-negligible anomalous dispersion in the mid-IR spectrum in AFM IR, though it is worth noting in that case the IR light was brought to the sample as an evanescent wave via ATR illumination.

With this caveat, both the peak area ratio analysis and PCA have provided evidence of an increased amount of phospholipid in the perinuclear region of the AM-treated cells, consistent with the DIPL phenotype. Similar regional differences were not observed in the nuclear and perinuclear regions of UT cells, indicating that the phospholipid signals were treatment-derived rather than the detection of lipid-rich cytosolic organelles, such as the endoplasmic reticulum.[7,24]

The SR-based RE-AFM-IR is designed to provide complementary capabilities to laser-based AFM-IR instruments, with the added advantage of simultaneous acquisition of full FTIR spectra across the midrange IR spectra. Focusing on studies with mammalian cells, laser-based AFM-IR nanospectroscopy has been used to acquire chemical signatures from subcellular regions in fibroblasts[25] and human colon adenocarcinoma cell lines,[26] as well as to investigate subcellular differences in erythrocytes subjected to oxidative stress,[27] malaria-infected erythrocytes,[21] protein clustering in chemically stressed HeLa cells,[18,28] changes to protein conformation in nanodiamond-treated rat hepatoma cells,[29] and the subcellular location of organometallic conjugates[30] in human breast cancer cells. The data generated in the current study using a model of DIPL in murine macrophage-like cells demonstrates that, like AFM-IR, the SR-based RE-AFM-IR end station at the MIRIAM beamline B22 can generate chemical information from FTIR spectral changes on subcellular regions at 100 nm scale.

In contrast to laser-based AFM-IR, where 100 mW of single wavelength photon power is available at the source and can be used in a ring-down sample excitation[31] or in RE-AFM-IR mode, the SR RE-AFM-IR method provides a total of <1 mW broadband photon flux onto the sample. This guarantees no radiation damage to the sample. However, due to the linearity of the absorption spectroscopy by SR, the detection of spectra with sufficient SNR from very thin sample regions (approximately <200 nm) was experimentally hindered here. The bottom illumination mode resulted in an altered amide I:amide II peak ratio, which has not been reported for AFM-IR instruments with top illumination. On the other hand, the full mid-IR spectrum and data set generated by the SR RE-AFM-IR instrument enabled a more in-depth chemometric analysis, similar to state-of-the-art analysis for microFTIR data. For example, it was possible to assess peak ratios from bands in distant spectral regions, such as the ν(C═O):3745−3020 cm^{-1} ratio, as well as carry out PCA on full mid-IR spectral data, both of which have limited applicability with the use of tunable IR laser AFM-IR techniques: the comparison of spectral regions obtained with different laser chips (QCL) or with different modes of lasers (OPO) is not fully reliable (e.g., issue of stitching different spectral ranges together).

■ CONCLUSIONS

In summary, SR-based RE-AFM-IR was shown here to be capable of directly measuring the entire mid-infrared FTIR absorption spectra of mammalian cells and their internal molecular composition at the 100 nm scale. The present study reports a first successful application of SR RE-AFM-IR to interrogate biological soft matter at the subcellular level, in this case on a cellular model of DIPL. IR vibrational maps across the whole cell confirmed the spatial resolution scale of 100 nm on a lateral scale, while a sample thickness of >200 nm was ideal for the generated photothermal spectra. Although the RE-AFM-IR spectra have an intrinsically lower signal-to-noise ratio

https://dx.doi.org/10.1021/acs.analchem.9b05759
Anal. Chem. 2020, 92, 8097−8107

compared to FTIR microspectroscopy, vibrational band assignment was possible, and all characteristic peaks for lipids, proteins, and DNA were identified. Chemometric analysis of RE-AFM-IR nanospectra generated from the nuclear and perinuclear regions of UT and AM-treated cells showed that the perinuclear cytoplasm of amiodarone-treated cells had significantly elevated band intensities in the regions corresponding to phosphate and carbonyl groups, indicating detection of phospholipid-rich inclusion bodies typical for cells with DIPL. The results of this study are of importance to demonstrate not only the applicability of SR-based RE-AFM-IR to characterize the soft biological matter with a subcellular spatial resolution but also that the FTIR spectral information gathered from an individual submicron sample volume enables chemometric identification of drug-treatment and biochemical discrimination between cells.

■ ASSOCIATED CONTENT

Supporting Information

The Supporting Information is available free of charge at https://pubs.acs.org/doi/10.1021/acs.analchem.9b05759.

Figure S1, optical images of large fields of view showing selected cells compared to cell population; Figure S2, AFM images showing locations of RE-AFM-IR measurements (red points and lines) for each cell; Figure S3, example of how carbonyl peak was calculated from spectra; and Figure S4, averaged SR RE-AFM-IR spectra from nuclear and perinuclear regions of UT and AM cells (PDF)

■ AUTHOR INFORMATION

Corresponding Author

Ka Lung Andrew Chan − *Institute of Pharmaceutical Sciences, School of Cancer and Pharmaceutical Science, King's College London, London SE1 9NH, U.K.;* orcid.org/0000-0002-1137-4599; Email: ka_lung.chan@kc.ac.uk

Authors

Ioannis Lekkas − *Diamond Light Source, Chilton-Didcot OX11 0DE, U.K.*

Mark D. Frogley − *Diamond Light Source, Chilton-Didcot OX11 0DE, U.K.*

Gianfelice Cinque − *Diamond Light Source, Chilton-Didcot OX11 0DE, U.K.;* orcid.org/0000-0001-6801-8010

Ali Altharawi − *Institute of Pharmaceutical Sciences, School of Cancer and Pharmaceutical Science, King's College London, London SE1 9NH, U.K.*

Gianluca Bello − *Institute of Synthetic Bioarchitectures, Department of Nanobiotechnology, University of Natural Resources and Life Sciences, Vienna, 1190 Vienna, Austria*

Lea Ann Dailey − *Department of Pharmaceutical Technology and Biopharmacy, University of Vienna, 1090 Vienna, Austria;* orcid.org/0000-0001-8220-5701

Complete contact information is available at: https://pubs.acs.org/10.1021/acs.analchem.9b05759

Author Contributions

This work is equally contributed to by the teams from the following three institutes: Diamond Light Source, University of Vienna, and King's College London.

Notes

The authors declare no competing financial interest.

■ ACKNOWLEDGMENTS

The authors would like to acknowledge Dr. Abhinav Kumar and Dr. Lysann Tietze for their assistance with the TEM and fluorescence microscopy. K.L.A.C. acknowledges EPSRC for support (EP/L013045/1). A.A. thanks Prince Sattam Bin Abdulaziz University (Saudi Arabia) for his Ph.D. sponsorship. Diamond Light Source is acknowledged for beamtime at the MIRIAM beamline B22-commissioning/collaborative call 2019 (SM21061). Finally we would like to thank the reviewers for their expert and insightful comments.

■ REFERENCES

(1) Donaldson, P. M.; Kelley, C. S.; Frogley, M. D.; Filik, J.; Wehbe, K.; Cinque, G. *Opt. Express* **2016**, *24*, 1852−1864.

(2) Dazzi, A.; Prater, C. B. *Chem. Rev.* **2017**, *117*, 5146−5173.

(3) Fu, W. Y.; Zhang, W. *Small* **2017**, *13*, 1603525.

(4) Carr, G. L. *Rev. Sci. Instrum.* **2001**, *72*, 1613−1619.

(5) Nasse, M. J.; Walsh, M. J.; Mattson, E. C.; Reininger, R.; Kajdacsy-Balla, A.; Macias, V.; Bhargava, R.; Hirschmugl, C. J. *Nat. Methods* **2011**, *8*, 413−416.

(6) Findlay, C. R.; Wiens, R.; Rak, M.; Sedlmair, J.; Hirschmugl, C. J.; Morrison, J.; Mundy, C. J.; Kansiz, M.; Gough, K. M. *Analyst* **2015**, *140*, 2493−2503.

(7) Chan, K. L. A.; Fale, P. L. V.; Atharawi, A.; Wehbe, K.; Cinque, G. *Anal. Bioanal. Chem.* **2018**, *410*, 6477−6487.

(8) Vongsvivut, J.; Pérez-Guaita, D.; Wood, B. R.; Heraud, P.; Khambatta, K.; Hartnell, D.; Hackett, M. J.; Tobin, M. J. *Analyst* **2019**, *144*, 3226−3238.

(9) Anderson, N.; Borlak, J. *FEBS Lett.* **2006**, *580*, 5533−5540.

(10) Ajaezi, G. C.; Eisele, M.; Contu, F.; Lal, S.; Rangel-Pozzo, A.; Mai, S.; Gough, K. M. *Analyst* **2018**, *143*, 5926−5934.

(11) Bechtel, H. A.; Muller, E. A.; Olmon, R. L.; Martin, M. C.; Raschke, M. B. *Proc. Natl. Acad. Sci. U. S. A.* **2014**, *111*, 7191−7196.

(12) Bakir, G.; Girouard, B. E.; Johns, R. W.; Findlay, C. R. J.; Bechtel, H. A.; Eisele, M.; Kaminskyj, S. G. W.; Dahms, T. E. S.; Gough, K. M. *Analyst* **2019**, *144*, 928−934.

(13) Cinque, G.; Frogley, M. D.; Wehbe, K.; Filik, J.; Pijanka, J. *Synchrotron radiation news* **2011**, *24*, 24−33.

(14) Cinque, G.; Frogley, M. D. Beamline Performance. https://www.diamond.ac.uk/Instruments/Soft-Condensed-Matter/B22/specs.html.

(15) Jarvis, R. M.; Broadhurst, D.; Johnson, H.; O'Boyle, N. M.; Goodacre, R. *Bioinformatics* **2006**, *22*, 2565−2566.

(16) Rosenberger, M. R.; Wang, M. C.; Xie, X.; Rogers, J. A.; Nam, S.; King, W. P. *Nanotechnology* **2017**, *28*, 355707.

(17) Kenkel, S.; Bhargava, R. Nanoscale imaging of biological samples with responsivity corrected Atomic Force Microscopy-Infrared (AFM-IR) spectroscopy. In *Nanoscale Imaging, Sensing, and Actuation for Biomedical Applications XVI*; Nicolau, D. V., Fixler, D., Goldys, E. M., Eds.; 2019; Vol. *10891*, DOI: 10.1117/12.2510131.

(18) Giliberti, V.; Baldassarre, L.; Rosa, A.; de Turris, V.; Ortolani, M.; Calvani, P.; Nucara, A. *Nanoscale* **2016**, *8*, 17560−17567.

(19) Kenkel, S.; Mittal, A.; Mittal, S.; Bhargava, R. *Anal. Chem.* **2018**, *90*, 8845−8855.

(20) Wrobel, T. P.; Bhargava, R. *Anal. Chem.* **2018**, *90*, 1444−1463.

(21) Perez-Guaita, D.; Kochan, K.; Batty, M.; Doerig, C.; Garcia-Bustos, J.; Espinoza, S.; McNaughton, D.; Heraud, P.; Wood, B. R. *Anal. Chem.* **2018**, *90*, 3140−3148.

(22) Kochan, K.; Perez-Guaita, D.; Pissang, J.; Jiang, J. H.; Peleg, A. Y.; McNaughton, D.; Heraud, P.; Wood, B. R. *J. R. Soc., Interface* **2018**, *15*, 20180115.

(23) Ramer, G.; Aksyuk, V. A.; Centrone, A. *Anal. Chem.* **2017**, *89*, 13524−13531.

(24) Gazi, E.; Dwyer, J.; Lockyer, N. P.; Miyan, J.; Gardner, P.; Hart, C. A.; Brown, M. D.; Clarke, N. W. *Vib. Spectrosc.* **2005**, *38*, 193−201.

(25) Quaroni, L.; Pogoda, K.; Wiltowska-Zuber, J.; Kwiatek, W. M. *RSC Adv.* **2018**, *8*, 2786−2794.

(26) Kennedy, E.; Al-Majmaie, R.; Al-Rubeai, M.; Zerulla, D.; Rice, J. H. *J. Biophotonics* **2015**, *8*, 133−141.
(27) Ruggeri, F. S.; Marcott, C.; Dinarelli, S.; Longo, G.; Girasole, M.; Dietler, G.; Knowles, T. P. J. *Int. J. Mol. Sci.* **2018**, *19*, 2582.
(28) Baldassarre, L.; Giliberti, V.; Rosa, A.; Ortolani, M.; Bonamore, A.; Baiocco, P.; Kjoller, K.; Calvani, P.; Nucara, A. *Nanotechnology* **2016**, *27*, 075101.
(29) Khanal, D.; Kondyurin, A.; Hau, H.; Knowles, J. C.; Levinson, O.; Ramzan, I.; Fu, D.; Marcott, C.; Chrzanowski, W. *Anal. Chem.* **2016**, *88*, 7530−7538.
(30) Policar, C.; Waern, J. B.; Plamont, M. A.; Clede, S.; Mayet, C.; Prazeres, R.; Ortega, J. M.; Vessieres, A.; Dazzi, A. *Angew. Chem., Int. Ed.* **2011**, *50*, 860−864.
(31) Dazzi, A.; Prater, C. B.; Hu, Q. C.; Chase, D. B.; Rabolt, J. F.; Marcott, C. *Appl. Spectrosc.* **2012**, *66*, 1365−1384.

https://dx.doi.org/10.1021/acs.analchem.9b05759
Anal. Chem. 2020, 92, 8097−8107